

1 Observational evidence of increasing global radiative forcing

2
3 Ryan J. Kramer^{1,2,*}, Haozhe He³, Brian J. Soden³, Lazaros Oreopoulos¹, Gunnar Myhre⁴,
4 Piers M. Forster⁵, Christopher J. Smith^{5,6}
5
6

7 ¹Earth Sciences Division, NASA Goddard Space Flight Center, Greenbelt, MD 20771, USA

8 ²Universities Space Research Association, 7178 Columbia Gateway Drive, Columbia, MD
9 21046, USA

10 ³Rosenstiel School of Marine and Atmospheric Science, University of Miami, 4600

11 Rickenbacker Causeway, Miami, FL 33149, USA

12 ⁴CICERO Center for International Climate and Environmental Research in Oslo, 0318, Oslo,
13 Norway

14 ⁵School of Earth and Environment, University of Leeds, Leeds, LS2 9JT, UK

15 ⁶International Institute for Applied Systems Analysis (IIASA), Laxenburg, 2351, Austria
16

17 Corresponding Author: Ryan J. Kramer (ryan.j.kramer@nasa.gov)

18
19 **Key Points**

- 20 • Observed instantaneous radiative forcing has increased, strengthening the top-of-
21 atmosphere radiative imbalance.
- 22 • Due to cancellations in longwave and shortwave radiation, the sum of rapid adjustments
23 and radiative feedbacks exhibit an insignificant trend.
- 24 • Observed increases in instantaneous radiative forcing are direct evidence of the
25 anthropogenic effects on the Earth's radiative energy budget.

26

27

28

29

30

31

32

33 **Abstract**

34

35 Changes in atmospheric composition, such as increasing greenhouse gases, cause an initial
36 radiative imbalance to the climate system, quantified as the instantaneous radiative forcing. This
37 fundamental metric has not been directly observed globally and previous estimates have come
38 from models. In part, this is because current space-based instruments cannot distinguish the
39 instantaneous radiative forcing from the climate's radiative response. We apply radiative kernels
40 to satellite observations to disentangle these components and find all-sky instantaneous radiative
41 forcing has increased 0.53 ± 0.11 W/m² from 2003 through 2018, accounting for positive trends in
42 the total planetary radiative imbalance. This increase has been due to a combination of rising
43 concentrations of well-mixed greenhouse gases and recent reductions in aerosol emissions. These
44 results highlight distinct fingerprints of anthropogenic activity in Earth's changing energy
45 budget, which we find observations can detect within 4 years.

46

47 **Plain Language Summary**

48 Climate change is a response to energy imbalances in the climate system. For example, rising
49 greenhouse gases directly cause an initial imbalance, the radiative forcing, in the planetary
50 radiation budget, and surface temperatures increase in response as the climate attempts to restore
51 balance. The radiative forcing and subsequent radiative feedbacks dictate the amount of
52 warming. While there are well-established observational records of greenhouse gas
53 concentrations and surface temperatures, there is not yet a global measure of the radiative
54 forcing, in part because current satellite observations of Earth's radiation only measure the sum
55 total of radiation changes that occur. We use the radiative kernel technique to isolate radiative

56 forcing from total radiative changes and find it has increased from 2003 through 2018,
57 accounting for nearly all of the long-term growth in the total top-of-atmosphere radiation
58 imbalance during this period. We confirm that rising greenhouse gas concentrations account for
59 most of the increases in the radiative forcing, along with reductions in reflective aerosols. This
60 serves as direct evidence that anthropogenic activity has affected Earth’s energy budget in the
61 recent past.

62
63 **1. Introduction**

64
65 The Instantaneous Radiative forcing (IRF) is the initial imbalance of the Earth’s top-of-
66 the-atmosphere (TOA) radiative energy budget directly caused by a change in atmospheric
67 composition, such as increasing greenhouse gases (GHGs), or perturbed surface properties, like
68 from land use change. All anthropogenic climate changes are a response to the IRF, including
69 surface temperature change and associated radiative feedbacks (Sherwood et al. 2015). Despite a
70 sound basis in physics and radiative transfer theory, the IRF is hard to directly diagnose from
71 observations. Multiple remote sensing and in-situ instruments observe net radiative fluxes, but
72 these measurements convolve the IRF with radiative responses to the changing atmospheric
73 state. Some studies have diagnosed a more broadly defined “greenhouse effect” by evaluating
74 observations of clear-sky longwave radiation at the surface (Philipona et al. 2004) and TOA
75 (Raghuraman et al. 2019), but this analysis does not separate the IRF from water vapor feedback
76 processes.

77 Harries et al. (2001) compared outgoing longwave radiation at the TOA from two
78 satellite instruments launched decades apart, attributing emission differences at relevant spectral
79 bands to rising greenhouse gas (GHG) concentrations. However, instrumental uncertainty
80 between the two platforms complicates interpretation (Jiang et al. 2011). Feldman et al. (2015,

81 2018) used ground observations from the US Department of Energy Atmospheric Radiation
82 Measurement (ARM) program to provide the most observationally-oriented assessment to date
83 of GHG surface radiative forcing, which is proportional to the TOA IRF. However, their
84 analysis was limited to longwave (LW) forcing from CO₂ and CH₄ and was only conducted for
85 two locations. The total IRF has not been directly diagnosed globally from observations.

86 Well understood radiative transfer theory tightly constraints the GHG component of the IRF.
87 Line-by-line radiative transfer models diagnose it within 1% agreement (Collins et al. 2006;
88 Mlynczak et al. 2016; Pincus et al. 2020). However, these highly accurate calculations are
89 computationally expensive, so analysis is often limited to a few idealized atmospheric profiles.
90 Quantifying the IRF globally and over time relies on more efficient but less accurate
91 parameterized radiative transfer models (Soden et al. 2018), which introduces model bias when
92 applied to observations. Diagnosing the IRF from aerosols with these models suffers from the
93 same pitfalls, plus additional uncertainty associated with aerosol optical properties that are not
94 well-observed (Randles et al. 2013; Stier et al. 2013). While there have been recent efforts to
95 constrain aerosol IRF with observations (Bellouin et al. 2020; Watson-Parris et al. 2020), results
96 are usually not temporally resolved.

97 Here we circumvent these limitations by applying radiative kernels (Soden et al. 2008) to
98 isolate the IRF from radiative feedbacks and rapid adjustments over time. We demonstrate that
99 the IRF has increased with rising GHG concentrations, accounting for recent, positive trends in
100 the total TOA radiative imbalance. More specifically, we consider this IRF to be largely a
101 consequence of concentration changes after anthropogenic emissions are moderated by natural
102 carbon cycle responses (Friedlingstein et al. 2019).

103

104 **2. Methods**

105
106 Variations in the total, all-sky radiative energy balance at the TOA, dR , constrain global
107 surface temperature change and consists of the all-sky instantaneous radiative forcing (IRF) and
108 radiative responses to the IRF:

109
110
$$dR = IRF + dR_\lambda \quad (1),$$

111
112
113 where dR_λ is net radiative changes caused by surface temperature-mediated radiative feedbacks
114 and rapid adjustments from, to first order, temperature (T), water vapor (q), surface albedo (α)
115 and cloud (C) changes (Vial et al. 2013; Sherwood et al. 2015):

116
117
$$dR_\lambda = dR_T + dR_q + dR_\alpha + dR_C \quad (2).$$

118
119 For simplicity, we will not decompose these terms further into feedbacks and rapid adjustments
120 since it has no bearing on diagnosing the IRF. We simply refer to these radiative anomalies as
121 radiative responses. We note that dR_λ includes both anthropogenic responses and natural
122 variability (e.g. Trenberth et al. 2015).

123 The Clouds and Earth's Radiant Energy System (CERES) has provided global TOA
124 energy balance observations since 2000. Here, we diagnose dR using radiative flux anomalies
125 from the CERES Energy Balance and Filled (EBAF) Ed. 4.1 product (Loeb et al. 2018a; Loeb et
126 al. 2019). While no observational product measures the radiative response terms in isolation,
127 they can be diagnosed using radiative kernels combined with observations of the relevant state

128 variable, x (B. Zhang et al. 2019; Bony et al. 2020). An individual, non-cloud radiative response,
129 dR_x , in linear form is:

130

$$131 \quad dR_x = \frac{\partial R}{\partial x} dx = K_x dx, \quad x = T, q, \alpha \quad (3),$$

132

133 where K_x is a radiative kernel representing direct radiative changes from small, standard
134 perturbations in state variable x and dx is the actual temperature (T), water vapor (q) or surface
135 albedo (α) climate response. Under clear-sky (CS) conditions:

$$136 \quad dR^{CS} = IRF^{CS} + dR_\lambda^{CS} \quad (4),$$

137

138 where:

$$139 \quad dR_\lambda^{CS} = dR_T^{CS} + dR_q^{CS} + dR_\alpha^{CS} \quad (5).$$

140

141 To diagnose dR_x or dR_x^{CS} we use observational-based radiative kernels developed from
142 the CloudSat Fluxes and Heating Rates product 2B-FLXHR-LIDAR (Kramer et al. 2019).
143 Unlike GCM-derived radiative kernels, these kernels are free from model bias in the base state,
144 and thus ideal for diagnosing observed radiation changes. Calculating K_x requires using a
145 radiative transfer model to convert base state perturbations to radiative sensitivities. Therefore,
146 using radiative kernels introduces some radiative-transfer model dependency. We apply the
147 radiative kernels to deseasonalized anomalies of temperature and specific humidity profiles from
148 version 6 Level 3 AIRS retrievals (Aumann et al. 2003) to estimate dR_T and dR_q and to surface
149 albedo anomalies from CERES EBAF surface fluxes (Kato et al. 2018) to estimate dR_α . Due to
150 computational expense, radiative kernels, including those used here, are often derived from one

151 year of data. However radiative kernel inter-annual variability is small (Pendergrass et al. 2018;
 152 Thorsen et al. 2018), therefore applying radiative kernels to the entire observational record is
 153 justified.

154 In the traditional radiative kernel technique used here, the cloud radiative response (dR_C)
 155 is calculated as the change in cloud radiative effects (CRE) corrected for cloud masking (Soden
 156 et al, 2008; Kramer et al. 2019):

$$158 \quad dR_C = dCRE - (dR_T - dR_T^{CS}) - (dR_q - dR_q^{CS}) - (dR_\alpha - dR_\alpha^{CS}) - (IRF - IRF^{CS}) \quad (6),$$

159
 160 where CRE is the difference between all-sky and clear-sky radiative fluxes. The cloud masking
 161 correction is necessary because CRE includes differences between all-sky and clear-sky non-
 162 cloud radiative changes, which are not actual cloud radiative responses (Soden et al. 2004). Here
 163 $dCRE$ is estimated using the TOA CERES EBAF radiative fluxes. The dR_x terms are diagnosed
 164 using all-sky and clear-sky radiative kernels as described above.

165 The ultimate goal of this study is to derive the IRF from these radiative kernel
 166 calculations. Under clear-sky conditions, we simply diagnose IRF^{CS} by rearranging Equation 3,
 167 whereby:

$$168 \quad IRF^{CS} = dR^{CS} - dR_\lambda^{CS} = dR^{CS} - (dR_T^{CS} + dR_q^{CS} + dR_\alpha^{CS}) \quad (7),$$

169
 170 For all-sky conditions, an analogous calculation would require dR_C to be removed from dR , but
 171 since estimating dR_C as in equation 6 requires the IRF to be known, this differencing technique is
 172 not possible. Following common practice (Soden et al. 2008; Vial et al. 2013), we estimate the
 173 all-sky IRF as:

174
$$IRF = \frac{IRF^{CS}}{Cl} \quad (8),$$

175
176 where Cl is a constant that accounts for cloud masking of the IRF. For the longwave (LW) Cl ,
177 we use a constant of 1.24, derived by dividing clear-sky and all-sky double-call radiative transfer
178 calculations of CO_2 IRF from models (Smith et al. 2018). The cloud mask for the shortwave
179 (SW) is derived from direct output of aerosol IRF from Modern-Era Retrospective Analysis for
180 Research and Applications, Version 2 (MERRA-2) reanalysis (Gelaro et al. 2017). The global-
181 mean value is 2.43, in line with a range of observational-based cloud masking estimates by
182 Bellouin et al. (2020). Only the MERRA-2 SW Cl is available over time, but it has an
183 insignificant long-term trend. Consequently, SW IRF has nearly identical trends when computed
184 with a time resolved versus constant SW Cl .

185 This conversion to all-sky conditions accounts for the presence of clouds but not cloud
186 changes. Therefore, the IRF in this study does not include aerosol-cloud interactions, such as
187 cloud albedo effects (Boucher et al. 2013). Instead, these terms are included in dR_C . Therefore,
188 the aerosol component to the kernel-derived estimates of IRF is akin to aerosol direct radiative
189 effects found throughout the literature (e.g. Thorsen et al. 2020).

190 The AIRS L3 data has the shortest record among satellite observations used in this study,
191 with 2003 being the first complete year of data. Thus, we compute all deseasonalized anomalies
192 from 2003 through 2018 relative to the mean of that time span. While we refer to the resulting
193 calculation as the IRF for brevity, we actually show anomalies of the IRF. For comparison, we
194 also estimate the IRF by applying the CloudSat radiative kernels to MERRA-2 reanalysis over
195 the same period. This reanalysis product assimilates a variety of satellite observations, including
196 observations of aerosol properties.

197 In climate models, idealized simulations and flux diagnostics from double-call radiative
198 transfer calculations can be used to evaluate the accuracy of radiative kernel estimates of dR_{λ} and
199 IRF (e.g. Vial et al. 2013; Smith et al. 2018). Such a comparison is not possible in the observed
200 record or the MERRA-2 reanalysis, however. Since the IRF is derived from differencing the
201 other radiative terms, there will always be near-perfect energy closure, albeit with some error due
202 to cloud masking assumptions, which is typically small (Chung and Soden 2015). Alternatively,
203 we will compare these kernel-derived estimates to various independent measures of the IRF.

204 To verify the aerosol component of the IRF, we compare radiative kernel-derived SW
205 IRF to direct output of the aerosol direct radiative effect from MERRA-2. We also compare SW
206 IRF to trends in aerosol optical depth (AOD) from MERRA-2 and observations from the
207 Moderate Resolution Imaging Spectroradiometer (MODIS) merged Dark Target and Deep Blue
208 product (Sayer et al. 2014).

209 We compare radiative-kernel derived estimates of the LW IRF to offline radiative
210 transfer calculations of GHG IRF. We apply empirical formulas to observed global-mean
211 concentrations of 5 major greenhouse gases (CO_2 , CH_4 , N_2O , CFC-11 and CFC-12), provided by
212 NOAA Global Monitoring Division (Hoffman et al. 2006; Montzka et al. 2011). Etminan et al.
213 (2016) derive the empirical formulas from polynomial fits to line-by-line radiative forcing
214 calculations. While these formulas were originally developed for net stratospherically adjusted
215 radiative forcing, we use corrections from additional line-by-line calculations (Hodnebrog et al.
216 2013; Etminan et al. 2016) to calculate TOA IRF, decomposed into a LW and SW component.

217 We also estimate GHG IRF using the SOCRATES offline radiative transfer model
218 (Edwards et al. 1996; Manners et al. 2015) with NOAA GHG concentrations and atmospheric
219 profiles from the MERRA-2 reanalysis. Like the other IRF estimates, these calculations are

220 presented in anomaly space with the seasonal cycle removed. The IRF from CFCs has decreased
221 recently, but this has been compensated for by a near equal increase from other halocarbons not
222 considered in empirical fit and SOCRATES calculations (Myhre et al. 2013a). To account for
223 this, we repeat these calculations with no CFC trend. This only modifies total GHG IRF trends
224 by <5%, however, so hereafter we focus on results without this assumption. The SOCRATES
225 IRF calculations are conducted under pristine, clear-sky conditions and converted to all-sky via
226 Equation 8, like the radiative kernel calculations.

227 The various inputs and assumptions detailed above can contribute uncertainty to the
228 estimated radiative changes. In a Supplemental Appendix we provide a comprehensive
229 uncertainty assessment in the IRF trends due to these contributors, including from observed dR ,
230 radiative kernels, and the cloud masking constant, Cl . We find these uncertainties are smaller
231 than the trend regression uncertainty associated with timeseries variability. Therefore, all trends
232 presented hereafter are provided with 95% confidence intervals (or roughly 2 standard errors
233 around the mean) associated with the least-squares linear regression. This is common practice
234 when diagnosing CERES trends (e.g. Loeb et al. 2018a,b).

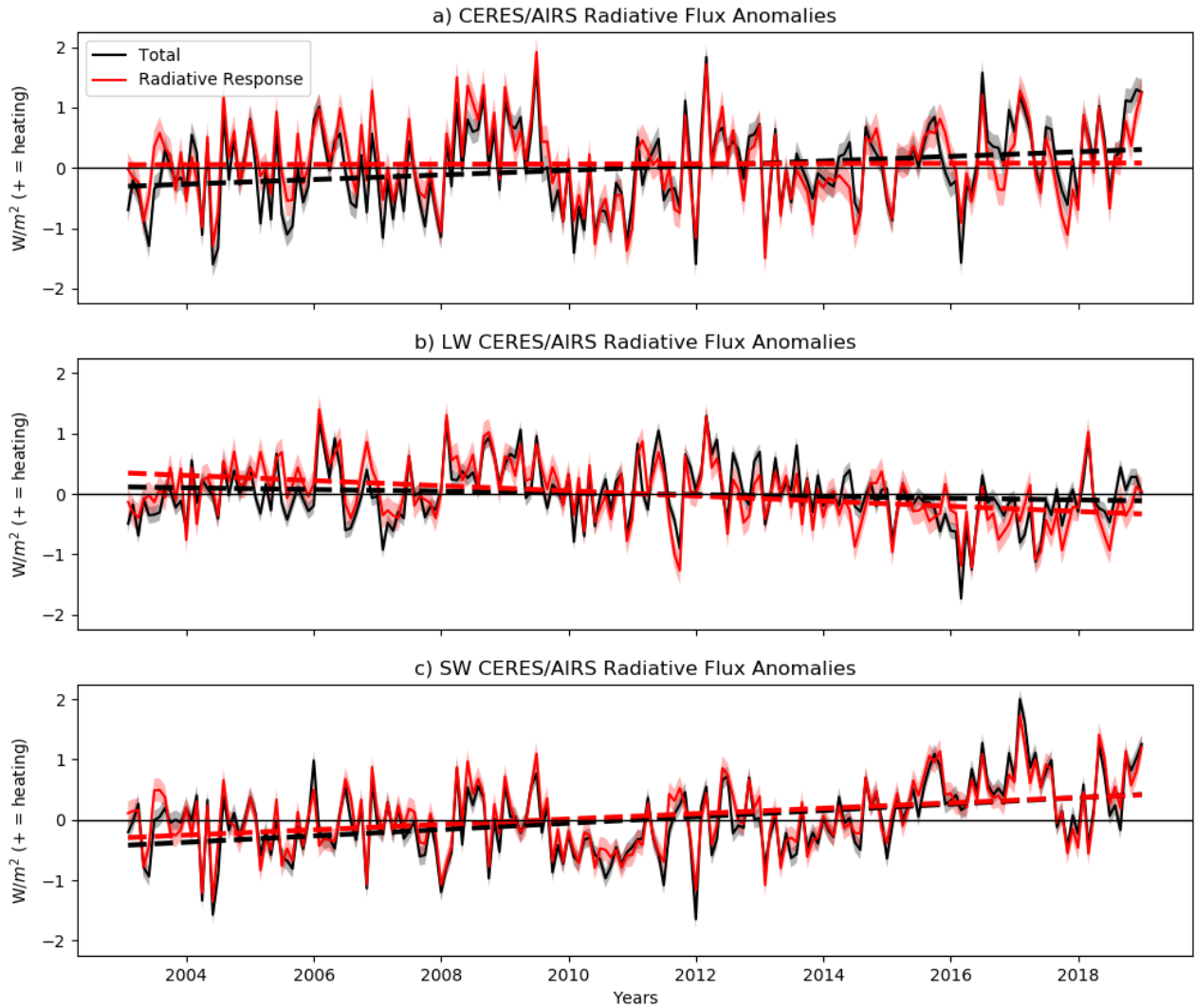
235 The anomalies of dR , dR_λ and the IRF are subject to the same sources of uncertainty as long-
236 term trends. Therefore, Figure 1 and 2 below include uncertainty bounds diagnosed as 2σ across
237 multiple estimates of the radiative terms using different radiative flux data products from CERES
238 and alternative radiative kernel sets and model estimates of Cl (see Supplemental Appendix).

239 240 **3. Results**

241
242
243 Figure 1a shows a timeseries of global-mean total radiative flux anomalies (dR) from CERES
244 satellite observations and its component from radiative responses (dR_λ), estimated by applying

245 the CloudSat-based radiative kernels to CERES and AIRS observations (hereafter
246 CERES/AIRS). Positive anomalies indicate a net increase in downwelling radiation at the TOA
247 (planetary warming). The sum of the radiative responses, dR_λ , accounts for nearly all of the total
248 short-term dR variability, as evident by their strong correlation ($r=0.88$) and small root-mean-
249 squared difference of 0.024 ± 0.003 W/m²; $\sim 3.5\%$ of the standard deviation of dR . On inter-annual
250 timescales, ENSO strongly influences this variability (Trenberth et al. 2014), which lags by ~ 5
251 months (Supplemental Fig. S1; Loeb et al. 2018b). Long-term dR exhibits a positive, linear trend
252 (0.038 ± 0.02 W/m²/year) significant with 95% confidence, while dR_λ exhibits an insignificant
253 trend (0.002 ± 0.02 W/m²/year) an order of magnitude smaller. This arises from cancelation
254 between LW and SW dR_λ . The LW dR_λ has a negative linear trend (-0.042 ± 0.02 W/m²/year)
255 (Fig. 1b), mainly from global warming-driven dR_T decreases (-0.041 ± 0.007 W/m²/year)
256 (Supplemental Fig. S2). The SW dR_λ trend (0.044 ± 0.02 W/m²/year) is nearly equal and opposite
257 of the LW, driven by increases in SW dR_α (0.023 ± 0.09 W/m²/year) and SW dR_C (0.020 ± 0.13
258 W/m²/year), a predominantly low cloud response (Loeb et al. 2018b). The latter alone accounts
259 for most of the SW interannual variability.

260



261

262

263 **Figure 1.** Global-mean a) net, b) longwave (LW) and c) shortwave (SW) total radiative flux
 264 anomalies from 2003 through 2018 as measured by CERES (black) and the contribution to that
 265 total from the sum of radiative responses (red). Respective trendlines are displayed as dashed
 266 lines. Uncertainty of $\pm 2\sigma$ is shown for each timeseries, computed as described in the Methods.
 267 Linear trends and 95% confidence intervals are provided in text.

268

269

270

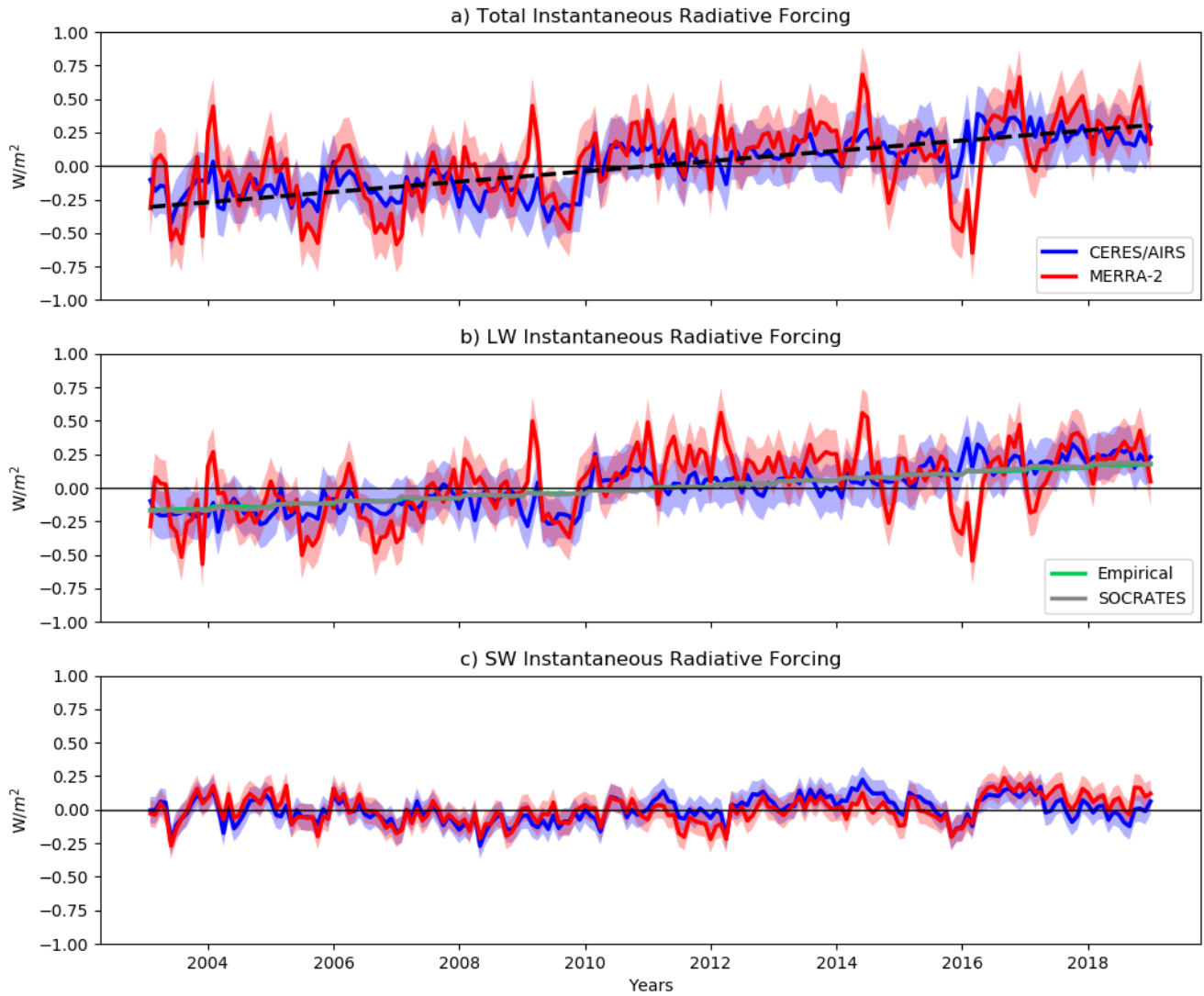
271

272

MERRA-2 also exhibits a significant, positive trend in dR but not dR_λ due to compensating
 LW and SW components (Supplemental Fig. S3). However, there is a positive trend in LW dR_λ
 and a negative trend in SW dR_λ , opposite from the CERES/AIRS response. This occurs due to a
 considerably different LW and SW dR_C (Supplemental Fig. S4) compared to satellite
 observations.

273 Since neither dR_λ or its uncertainties account for the positive dR trend, it must be
274 explained by the IRF. Figure 2 shows the timeseries of the total, LW and SW IRF under all-sky
275 conditions, estimated from the radiative kernel technique. The total CERES/AIRS IRF exhibits a
276 significant, positive trend (0.033 ± 0.007 W/m²/year), mostly from increasing LW IRF
277 (0.027 ± 0.006 W/m²/year). The SW IRF exhibits a smaller, yet still significant increase
278 (0.006 ± 0.003 W/m²/year). The LW IRF trend is opposite in sign from LW dR , since decreasing
279 LW dR_λ compensates. In the SW, IRF and dR are both increasing, but SW dR_λ is the dominant
280 contributor while the IRF trend is much smaller.

281 Rising GHG concentrations explain the positive LW IRF trend. Accordingly, it increases
282 at a similar rate to the GHG IRF estimates from the empirical fit (0.021 ± 0.0002 W/m²/year or
283 0.022 ± 0.0002 W/m²/year if ignoring CFCs [see Methods]) and the SOCRATES radiative
284 transfer model (0.023 ± 0.0003 W/m²/year) (Fig. 2b), despite these calculations neglecting some
285 GHG forcers found in nature, such as ozone. MERRA-2 exhibits a similar LW IRF trend to
286 CERES/AIRS (0.029 ± 0.003 W/m²/year) while direct output of the LW aerosol IRF from
287 MERRA-2 exhibits no trend. This further indicates GHG increases account for roughly all LW
288 IRF increases.



289

290

291 **Figure 2.** Global-mean a) total, b) longwave (LW) and c) shortwave (SW) instantaneous
 292 radiative forcing (IRF) estimated from the radiative kernel technique for CERES/AIRS (red) and
 293 MERRA-2 (blue). Additional calculations of greenhouse gas-only IRF are also shown using
 294 empirical formulas (green) and the SOCRATES radiative transfer model (gray). For reference,
 295 the trendline for total radiative flux anomalies (Fig 1a) is displayed with the total IRF as a black
 296 dashed line. Uncertainty of $\pm 2\sigma$ is shown with shading for each timeseries, computed as
 297 described in the Methods. Linear trends and 95% confidence intervals are provided in text and
 298 in Table 1.

299

Increasing GHG concentrations also contribute (0.002 ± 0.00 W/m²/year) to the total

300

positive SW IRF trends, according to estimates from the empirical fits. The SW GHG trend is

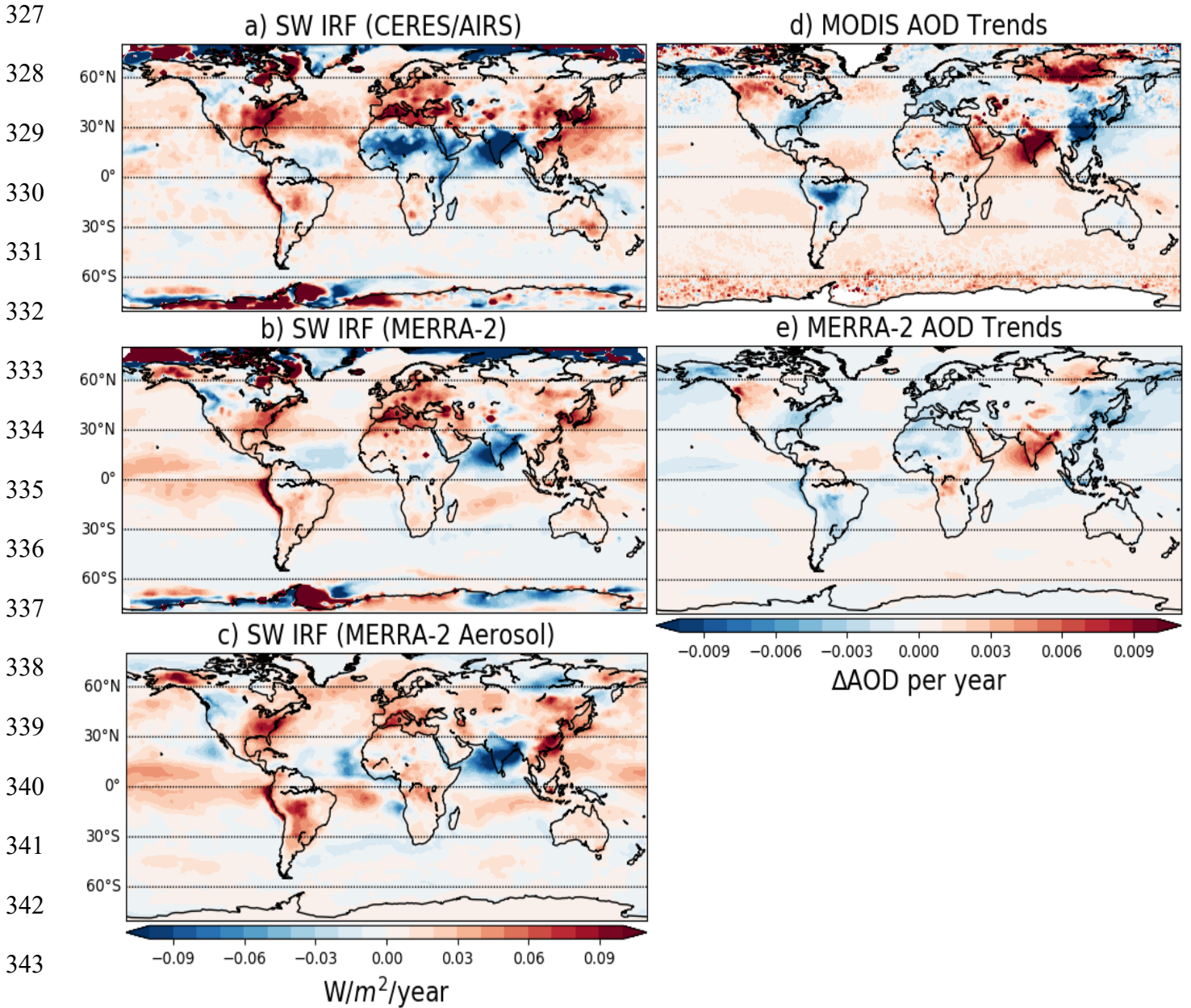
301 negligible in the SOCRATES calculations, but the model version used here does not account for
302 the SW absorption of CH₄.

303 The total SW IRF increase is nearly identical in CERES/AIRS and MERRA-2, and to
304 aerosol-only SW IRF trends from MERRA-2 direct output (Supplemental Fig. S5). They also
305 exhibit similar short-term variability. This suggests aerosols explain most of the SW IRF. The
306 long-term radiative heating is consistent with declining anthropogenic aerosol emissions during
307 this period (Q. Zhang et al. 2019). Towards the end of the timeseries, CERES/AIRS SW IRF has
308 more positive anomalies. Locally, the largest differences with MERRA-2 after 2015 are in major
309 absorbing aerosol source regions (Supplemental Fig. S6), suggesting a contribution from
310 different absorbing aerosol properties.

311 Figure 3 shows local linear trends in kernel-derived, total SW IRF from CERES/AIRS
312 and MERRA-2 and direct MERRA-2 output of aerosol-only SW IRF (Figure 3c). The spatial
313 pattern of the SW IRF trend is generally consistent across all three estimates. A notable
314 hemispheric asymmetry is present, with large changes concentrated in the populous Northern
315 Hemisphere. This includes large positive trends over the Eastern United States, Western Europe
316 and Eastern China, where anthropogenic emissions of reflective aerosols have declined because
317 of government actions to combat poor air quality (Kühn et al. 2014; Ridley et al. 2018; Q. Zhang
318 et al. 2019). In contrast, the SW IRF trends are negative over India, where emissions continue to
319 rise (Dey et al. 2012).

320 There are some magnitude differences in these major source regions, however. For
321 instance, trends are larger in the Eastern US and India in CERES/AIRS than in MERRA-2. This
322 coincides with differences in the MODIS and MERRA-2 AOD trends (Figure 3d,e), which are
323 also larger in CERES/AIRS. Over Saharan Africa, the sign of the SW IRF trend differs,

324 consistent with opposing trends in MODIS and MERRA-2 AOD. Dust radiative forcing during
325 this period is likely a key factor (Supplemental Fig. S7; Shao et al. 2013) and is highly uncertain
326 (Miller et al. 2014; Kok et al. 2017).



345 **Figure 3.** Local linear trends from 2003 through 2018 in all-sky shortwave instantaneous radiative forcing
346 (SW IRF) diagnosed in a) CERES/AIRS observations and b) MERRA-2 reanalysis using the radiative kernel
differencing technique and c) from direct output of MERRA-2 aerosol IRF. Also, local linear trends over the
same time period are shown for aerosol optical depth (AOD) from d) MODIS and e) MERRA-2.

347
348
349 The strong agreement in MERRA-2 trends from kernel differencing versus direct SW
350 aerosol IRF output (Fig 3b,c) highlights the dominant role of aerosols in the total SW IRF trends.
351 It also confirms the accuracy of the radiative kernel technique. The kernel differencing method
352 results in artifacts in the polar regions, however, where large local trends are a consequence of
353 underestimating the SW dR_{α} removed from dR (Supplemental Fig. S8) and not from actual
354 forcing. One possible explanation is surface albedo radiative kernels fail to capture important
355 ice-albedo feedback non-linearities (Block and Mauritsen 2013). Nevertheless, the polar region
356 errors have negligible effect on global-mean SW IRF trends.

357 Some inter- and intra-annual variability (hereafter short-term variability) in SW IRF is
358 expected, given natural variations in aerosol concentrations. Consequently, the detrended
359 aerosol-only ($\sigma=0.088$ W/m²) and kernel-derived ($\sigma=0.097$ W/m²) SW IRF in MERRA-2
360 exhibit similar variability and are highly correlated ($r=0.78$). The source of the notable short-
361 term variability in LW IRF (Fig. 2b) is less apparent, however, since greenhouse gas
362 concentrations increase relatively steadily on these timescales, as evident in the empirical fit
363 estimate of GHG IRF, which increases almost perfectly linearly.

364 While radiative kernel error may play some role, the LW IRF from CERES/AIRS
365 exhibits considerably more short-term variability ($\sigma=0.24$) than MERRA-2 ($\sigma=0.16$), despite
366 using the same CloudSat-derived radiative kernels in both estimates. This highlights short-term
367 inconsistencies between the radiative fluxes observed by CERES (dR^{cs}) and the AIRS retrievals
368 used to diagnose LW dR_{λ}^{cs} . For instance, the difference between CERES/AIRS and MERRA-2
369 dR_{λ}^{cs} exhibits considerably more short-term variability than the difference between dR^{cs} . This is
370 mostly due to different variability in dR_{τ}^{cs} (Supplemental Fig. S9), and more specifically due to

371 different temperature anomalies at the surface and in the boundary layer between AIRS and
372 MERRA-2 (Supplemental Fig. S10). Since AIRS temperature anomalies are more variable, so is
373 the dR_T^{cs} estimate. And since this variability is not also observed radiatively by CERES, it is not
374 evident in dR^{cs} . This ultimately translates to a more variable LW IRF when using the kernel
375 differencing technique. This also explains why LW IRF spatial patterns are noisier for
376 CERES/AIRS than for MERRA-2 (Supplemental Fig. S11). Cloud contamination likely
377 contributes to the AIRS temperature variability, as found previously (Hearty et al. 2014). This is
378 evident at the surface, for example, where the largest differences between AIRS and MERRA-2
379 temperature anomalies tend to occur where clouds are common (Supplemental Fig. S9),
380 especially over land. While global-mean surface temperature anomalies from AIRS closely agree
381 with other, independent datasets (Susskind et al. 2019), it is possible the temperature biases that
382 do exist are magnified in the context of radiative changes.

383 The LW IRF variability may also stem from its sensitivity to the atmospheric base state
384 (Pincus et al. 2015). However, this contribution appears to be small. In the LW GHG IRF
385 estimated from the SOCRATES radiative transfer model, we use daily MERRA-2 temperature,
386 surface albedo and humidity data, thus capturing the GHG IRF sensitivity to the unperturbed,
387 non-cloud base state. Still, the short-term variability from this offline calculation is nearly as
388 small as estimates with the empirical fit, which does not account for base state variability. The
389 LW IRF short-term variability in this comparison (and in the radiative kernel-derived estimates)
390 is not due to variations in the cloud base state since LW cloud masking is always treated as a
391 constant. While clouds may play a greater role in reality, the SW IRF estimated from radiative
392 kernels with constant cloud masking has similar short-term variability to the aerosol-only SW
393 IRF in MERRA-2, which accounts for cloud masking temporal variations. This suggests cloud

394 variability may not be important in the global-mean. Lastly, some LW IRF variability in
 395 MERRA-2 (and in CERES/AIRS) may be due to spatial variability in the GHG concentrations
 396 (Myhre et al. 2013a), which is not present in the empirical fit or the SOCRATES estimates.

397

	LW	SW	Net
CERES/AIRS	0.027±0.006	0.006±0.003	0.033±0.007
MERRA-2	0.029±0.003	0.006±0.003	0.035±0.004
Aerosol-Only MERRA-2	-4.2E-4±1.5E-4	0.006±0.003	0.006±0.003

398 **Table 1.** Global-mean linear trends ($W/m^2/year$) and 95% confidence bounds in
 399 instantaneous radiative forcing estimated using the radiative kernel differencing
 400 technique (first two rows) and MERRA-2 flux diagnostics (third row).

401

402

403

404

4. Conclusions

405

406 We have diagnosed the global instantaneous radiative forcing (IRF) directly from
 407 observations using radiative kernels. Table 1 summarizes linear trends. We find that from 2003
 408 through 2018, the observed IRF has increased $0.53 \pm 0.11 W/m^2$, almost entirely accounting for
 409 the positive trend in CERES Top-of-Atmosphere (TOA) radiative flux anomalies (dR). The
 410 intrinsic LW and SW climate radiative responses largely cancel out. This IRF increase mostly
 411 occurs in the LW ($0.43 \pm 0.1 W/m^2$), driven by rising greenhouse gas concentrations. This serves
 412 as direct observational evidence that anthropogenic activity is impacting the Earth's energy
 413 balance. The SW IRF has also increased ($0.1 \pm 0.05 W/m^2$). In part, this is a reflection of
 414 government-mandated aerosol emission reductions throughout major source regions, which may
 415 have a greater direct impact than inferred by the SW IRF, which does not include aerosol cloud-
 416 albedo effects in this analysis.

417 Diagnosing the observed IRF is important for our fundamental understanding of Earth's
418 response to climate change and a valuable piece of information for policy decisions.
419 Conceivably, observed IRF could be used as a top-down approach for monitoring the climate
420 response to mitigation efforts. By applying published metrics of instrumental uncertainty in
421 AIRS (Tobin et al. 2006; Hearty et al. 2014) and CERES (Loeb et al. 2018a), along with the
422 kernel-derived IRF variance and trend, we apply formulas by Leroy et al. (2008) to determine the
423 minimum length of the observational record necessary to detect a climate change signal. These
424 formulas account for trend uncertainty due to natural variability and instrumental uncertainty.
425 Using this approach, we find total IRF trends are detectable, given these sources of uncertainty,
426 within 3.8 years using the satellite data presented in this study. Therefore, the methods
427 introduced here could be useful for near-real time monitoring, especially since the time to
428 detection shortens with the lengthening of the observational record.

429

430 **Acknowledgements:** We thank the Editor, reviewers and Graeme Stephens for valuable
431 feedback on this work. RJK is supported by an appointment to the NASA Postdoctoral Program
432 administered by Universities Space Research Association. HH and BJS are supported by NASA
433 award 80NSSC18K1032. LO gratefully acknowledges support from NASA's
434 CloudSat/CALIPSO Science Team and MEaSUREs programs. GM, PMF and CJS were
435 supported by European Union's Horizon 2020 Research and Innovation Programme under grant
436 agreement no. 820829 (CONSTRAIN). PMF and CJS were also supported by UKRI NERC
437 grant NE/N006038/1 (SMURPHS). C.J.S. was supported by a NERC/IASA Collaborative
438 Research Fellowship (NE/T009381/1).

439

440 **Competing Interests:** Authors have no competing interests.

441

442 **Data and Materials Availability:** The CERES radiative flux observations are available at
443 <https://ceres.larc.nasa.gov/data/>. The AIRS temperature and water vapor observations and the
444 MERRA-2 reanalysis data are available at <https://disc.gsfc.nasa.gov/>. The CloudSat/CALIPSO
445 radiative kernels used in this study and related code for applying them are available at
446 <https://climate.rsmas.miami.edu/data/radiative-kernels/>.

447

448 **References**

449

450 Aumann, H.H., Chahine, M.T., Gautier, C., M. Goldberg, D., Kalnay, E., McMillin, L.M., et al.
451 (2003). AIRS/AMSU/HSB on the Aqua mission: design, science objectives, data products, and
452 processing systems. *IEEE Transactions on Geoscience and Remote Sensing*, 41(2), 253–264.
453 <https://doi.org/10.1109/TGRS.2002.808356>

454

455 Bellouin, N., Quaas, J., Gryspeerdt, E., Kinne, S., Stier, P., Watson-Parris, D., et al. (2020).
456 Bounding Global Aerosol Radiative Forcing of Climate Change. *Reviews of Geophysics*, 58(1),
457 e2019RG000660. <https://doi.org/10.1029/2019RG000660>

458

459 Block, K., & Mauritsen, T. (2013). Forcing and feedback in the MPI-ESM-LR coupled model
460 under abruptly quadrupled CO₂. *Journal of Advances in Modeling Earth Systems*, 5(4), 676–691.
461 <https://doi.org/10.1002/jame.20041>

462

463 Bony, S., Semie, A., Kramer, R. J., Soden, B., Tompkins, A. M., & Emanuel, K. A. (2020).
464 Observed Modulation of the Tropical Radiation Budget by Deep Convective Organization and
465 Lower-Tropospheric Stability. *AGU Advances*, 1(3). <https://doi.org/10.1029/2019AV000155>

466

467 Boucher, O., Randall, D., Artaxo, P., Bretherton, C., Feingold, G., Forster, P., et al., (2013)
468 Clouds and aerosols. In *Climate Change 2013: The Physical Science Basis. Contribution of*
469 *Working Group I to the Fifth Assessment Report of the Intergovernmental Panel on Climate*
470 *Change*. T.F. Stocker, D. Qin, G.-K. Plattner, M. Tignor, S.K. Allen, J. Doschung, A. Nauels, Y.
471 Xia, V. Bex, and P.M. Midgley, Eds. Cambridge University Press, pp. 571-657,
472 doi:10.1017/CBO9781107415324.016.

473

474 Chung, E.-S., & Soden, B. J. (2015). An Assessment of Direct Radiative Forcing, Radiative
475 Adjustments, and Radiative Feedbacks in Coupled Ocean–Atmosphere Models*. *Journal of*
476 *Climate*, 28(10), 4152–4170. <https://doi.org/10.1175/JCLI-D-14-00436.1>

477

478 Collins, W. D., Ramaswamy, V., Schwarzkopf, M. D., Sun, Y., Portmann, R. W., Fu, Q., et al.
479 (2006). Radiative forcing by well-mixed greenhouse gases: Estimates from climate models in the
480 Intergovernmental Panel on Climate Change (IPCC) Fourth Assessment Report (AR4). *Journal*
481 *of Geophysical Research*, 111(D14), D14317. <https://doi.org/10.1029/2005JD006713>
482

483 Dey, S., Di Girolamo, L., van Donkelaar, A., Tripathi, S. N., Gupta, T., & Mohan, M. (2012).
484 Variability of outdoor fine particulate (PM_{2.5}) concentration in the Indian Subcontinent: A
485 remote sensing approach. *Remote Sensing of Environment*, 127, 153–161.
486 <https://doi.org/10.1016/j.rse.2012.08.021>
487

488 Edwards, J. M., & Slingo, A. (1996). Studies with a flexible new radiation code. I: Choosing a
489 configuration for a large-scale model. *Quarterly Journal of the Royal Meteorological Society*,
490 122(531), 689–719. <https://doi.org/10.1002/qj.49712253107>
491

492 Etminan, M., Myhre, G., Highwood, E. J., & Shine, K. P. (2016). Radiative forcing of carbon
493 dioxide, methane, and nitrous oxide: A significant revision of the methane radiative forcing.
494 *Geophysical Research Letters*, 43(24), 12,614–12,623. <https://doi.org/10.1002/2016GL071930>
495

496 Feldman, D. R., Collins, W. D., Gero, P. J., Torn, M. S., Mlawer, E. J., & Shippert, T. R. (2015).
497 Observational determination of surface radiative forcing by CO₂ from 2000 to 2010. *Nature*,
498 519(7543), 339–343. <https://doi.org/10.1038/nature14240>
499

500 Feldman, D. R., Collins, W. D., Biraud, S. C., Risser, M. D., Turner, D. D., Gero, P. J., et al.
501 (2018). Observationally derived rise in methane surface forcing mediated by water vapour
502 trends. *Nature Geoscience*, 11(4), 238–243. <https://doi.org/10.1038/s41561-018-0085-9>
503

504 Friedlingstein, P., Jones, M. W., O’Sullivan, M., Andrew, R. M., Hauck, J., Peters, G. P., et al.
505 (2019). Global Carbon Budget 2019. *Earth System Science Data*, 11(4), 1783–1838.
506 <https://doi.org/10.5194/essd-11-1783-2019>
507

508 Gelaro, R., McCarty, W., Suárez, M. J., Todling, R., Molod, A., Takacs, L., et al. (2017). The
509 Modern-Era Retrospective Analysis for Research and Applications, Version 2 (MERRA-2).
510 *Journal of Climate*, 30(14), 5419–5454. <https://doi.org/10.1175/JCLI-D-16-0758.1>
511

512 Harries, J. E., Brindley, H. E., Sagoo, P. J., & Bantges, R. J. (2001). Increases in greenhouse
513 forcing inferred from the outgoing longwave radiation spectra of the Earth in 1970 and 1997.
514 *Nature*, 410(6826), 355–357. <https://doi.org/10.1038/35066553>
515

516 Hearty, T. J., Savtchenko, A., Tian, B., Fetzer, E., Yung, Y. L., Theobald, M., et al. (2014).
517 Estimating sampling biases and measurement uncertainties of AIRS/AMSU-A temperature and
518 water vapor observations using MERRA reanalysis. *Journal of Geophysical Research:*
519 *Atmospheres*, 119(6), 2725–2741. <https://doi.org/10.1002/2013JD021205>
520

521 Hodnebrog, Ø., Etminan, M., Fuglestad, J. S., Marston, G., Myhre, G., Nielsen, C. J., et al.
522 (2013). Global warming potentials and radiative efficiencies of halocarbons and related

523 compounds: A comprehensive review. *Reviews of Geophysics*, 51(2), 300–378.
524 <https://doi.org/10.1002/rog.20013>
525
526 Hofmann, D. J., Butler, J. H., Dlugokencky, E. J., Elkins, J. W., Masarie, K., Montzka, S. A., &
527 Tans, P. (2006). The role of carbon dioxide in climate forcing from 1979 to 2004: introduction of
528 the Annual Greenhouse Gas Index. *Tellus B: Chemical and Physical Meteorology*, 58(5), 614–
529 619. <https://doi.org/10.1111/j.1600-0889.2006.00201.x>
530
531 Jiang, Y., Aumann, H.H., Wingyee-Lau, M., & Yung, Y.L. (2011). Climate change sensitivity
532 evaluation from AIRS and IRIS measurements. *Proc. SPIE* 8153, XVI (2011), doi:
533 <http://dx.doi.org/10.1117/12.892817>
534
535 Kato, S., Rose, F. G., Rutan, D. A., Thorsen, T. J., Loeb, N. G., Doelling, D. R., et al. (2018).
536 Surface Irradiances of Edition 4.0 Clouds and the Earth’s Radiant Energy System (CERES)
537 Energy Balanced and Filled (EBAF) Data Product. *Journal of Climate*, 31(11), 4501–4527.
538 <https://doi.org/10.1175/JCLI-D-17-0523.1>
539
540 Kok, J. F., Ridley, D. A., Zhou, Q., Miller, R. L., Zhao, C., Heald, C. L., et al. (2017). Smaller
541 desert dust cooling effect estimated from analysis of dust size and abundance. *Nature*
542 *Geoscience*, 10(4), 274–278. <https://doi.org/10.1038/ngeo2912>
543
544 Kramer, R. J., Matus, A. V., Soden, B. J., & L’Ecuyer, T. S. (2019). Observation-Based
545 Radiative Kernels From CloudSat/CALIPSO. *Journal of Geophysical Research: Atmospheres*,
546 2018JD029021. <https://doi.org/10.1029/2018JD029021>
547
548 Kühn, T., Partanen, A.-I., Laakso, A., Lu, Z., Bergman, T., Mikkonen, S., et al. (2014). Climate
549 impacts of changing aerosol emissions since 1996. *Geophysical Research Letters*, 41(13), 4711–
550 4718. <https://doi.org/10.1002/2014GL060349>
551
552 Leroy, S.S., Anderson, J.G., & Ohring, G. (2008) Climate Signal Detection Times and
553 Constraints on Climate Benchmark Accuracy Requirements. *Journal of Climate*. 21, 841–846
554
555 Loeb, N. G., Doelling, D. R., Wang, H., Su, W., Nguyen, C., Corbett, J. G., et al. (2018a).
556 Clouds and the Earth’s Radiant Energy System (CERES) Energy Balanced and Filled (EBAF)
557 Top-of-Atmosphere (TOA) Edition-4.0 Data Product. *Journal of Climate*, 31(2), 895–918.
558 <https://doi.org/10.1175/JCLI-D-17-0208.1>
559
560 Loeb, N., Thorsen, T., Norris, J., Wang, H., & Su, W. (2018b) Changes in Earth’s Energy
561 Budget during and after the “Pause” in Global Warming: An Observational
562 Perspective, *Climate* 6, 62.
563
564 Loeb, N. G., Rose, F. G., Kato, S., Rutan, D. A., Su, W., Wang, H., et al. (2019). Toward a
565 Consistent Definition between Satellite and Model Clear-Sky Radiative Fluxes. *Journal of*
566 *Climate*, 33(1), 61–75. <https://doi.org/10.1175/JCLI-D-19-0381.1>
567

568 Manners J, Edwards JM, Hill P, Thelen J-C. (2015). SOCRATES (Suite Of Community
569 Radiative Transfer codes based on Edwards and Slingo) Technical Guide. Met Office, UK.
570

571 Miller, R. L., Knippertz, P., Pérez García-Pando, C., Perlwitz, J. P., & Tegen, I. (2014). Impact
572 of Dust Radiative Forcing upon Climate. In P. Knippertz & J.-B. W. Stuut (Eds.), *Mineral Dust:
573 A Key Player in the Earth System* (pp. 327–357). Dordrecht: Springer Netherlands.
574 https://doi.org/10.1007/978-94-017-8978-3_13
575

576 Mlynczak, M. G., Daniels, T. S., Kratz, D. P., Feldman, D. R., Collins, W. D., Mlawer, E. J., et
577 al. (2016). The spectroscopic foundation of radiative forcing of climate by carbon dioxide.
578 *Geophysical Research Letters*, 43(10), 5318–5325. <https://doi.org/10.1002/2016GL068837>
579

580 Montzka, S. A., Dlugokencky, E. J., & Butler, J. H. (2011). Non-CO2 greenhouse gases and
581 climate change. *Nature*, 476(7358), 43–50. <https://doi.org/10.1038/nature10322>
582

583 Myhre, G., Shindell, D., Bréon, F.-M., Collins, W., Fuglestedt, J., Huang, J., Koch, D.,
584 Lamarque, J.-F., Lee, E., et al., (2013a). Anthropogenic and natural radiative forcing. In *Climate
585 Change 2013: The Physical Science Basis. Contribution of Working Group I to the Fifth
586 Assessment Report of the Intergovernmental Panel on Climate Change*. T.F. Stocker, D. Qin, G.-
587 K. Plattner, M. Tignor, S.K. Allen, J. Doschung, A. Nauels, Y. Xia, V. Bex, and P.M. Midgley,
588 Eds. Cambridge University Press, pp. 659-740, doi:10.1017/CBO9781107415324.018
589

590 Myhre, G., Samset, B. H., Schulz, M., Balkanski, Y., Bauer, S., Bernsten, T. K., et al. (2013b).
591 Radiative forcing of the direct aerosol effect from AeroCom Phase II simulations. *Atmospheric
592 Chemistry and Physics*, 13(4), 1853–1877. <https://doi.org/10.5194/acp-13-1853-2013>
593

594 Pendergrass, A. G., Conley, A., & Vitt, F. M. (2018). Surface and top-of-atmosphere radiative
595 feedback kernels for CESM-CAM5. *Earth System Science Data*, 10(1), 317–324.
596 <https://doi.org/10.5194/essd-10-317-2018>
597

598 Philipona, R., Dürr, B., Marty, C., Ohmura, A., & Wild, M. (2004). Radiative forcing - measured
599 at Earth's surface - corroborate the increasing greenhouse effect. *Geophysical Research Letters*,
600 31(3). <https://doi.org/10.1029/2003GL018765>
601

602 Pincus, R., Mlawer, E. J., Oreopoulos, L., Ackerman, A. S., Baek, S., Brath, M., et al. (2015).
603 Radiative flux and forcing parameterization error in aerosol-free clear skies. *Geophysical
604 Research Letters*, 42(13), 5485–5492. <https://doi.org/10.1002/2015GL064291>
605

606 Pincus, R., Buehler, S. A., Brath, M., Jamil, O., Evans, F., Manners, J., et al. (2020). Benchmark
607 calculations of radiative forcing by greenhouse gases. *Earth and Space Science Open Archive*,
608 15. <https://doi.org/10.1002/essoar.10501550.1>
609

610 Randles, C. A., Kinne, S., Myhre, G., Schulz, M., Stier, P., Fischer, J., et al. (2013).
611 Intercomparison of shortwave radiative transfer schemes in global aerosol modeling: results from
612 the AeroCom Radiative Transfer Experiment. *Atmospheric Chemistry and Physics*, 13(5), 2347–
613 2379. <https://doi.org/10.5194/acp-13-2347-2013>

614
615 Raghuraman, S. P., Paynter, D., & Ramaswamy, V. (2019). Quantifying the Drivers of the Clear
616 Sky Greenhouse Effect, 2000–2016. *Journal of Geophysical Research: Atmospheres*, 124(21),
617 11354–11371. <https://doi.org/10.1029/2019JD031017>
618
619 Ridley, D. A., Heald, C. L., Ridley, K. J., & Kroll, J. H. (2018). Causes and consequences of
620 decreasing atmospheric organic aerosol in the United States. *Proceedings of the National*
621 *Academy of Sciences*, 115(2), 290. <https://doi.org/10.1073/pnas.1700387115>
622
623 Sayer, A. M., Munchak, L. A., Hsu, N. C., Levy, R. C., Bettenhausen, C., & Jeong, M.-J. (2014).
624 MODIS Collection 6 aerosol products: Comparison between Aqua’s e-Deep Blue, Dark Target,
625 and “merged” data sets, and usage recommendations. *Journal of Geophysical Research:*
626 *Atmospheres*, 119(24), 13,965–13,989. <https://doi.org/10.1002/2014JD022453>
627
628 Shao, Y., Klose, M., & Wyrwoll, K.-H. (2013). Recent global dust trend and connections to
629 climate forcing. *Journal of Geophysical Research: Atmospheres*, 118(19), 11,107–11,118.
630 <https://doi.org/10.1002/jgrd.50836>
631
632 Sherwood, S. C., Bony, S., Boucher, O., Bretherton, C., Forster, P. M., Gregory, J. M., &
633 Stevens, B. (2015). Adjustments in the Forcing-Feedback Framework for Understanding Climate
634 Change. *Bulletin of the American Meteorological Society*, 96(2), 217–228.
635 <https://doi.org/10.1175/BAMS-D-13-00167.1>
636
637 Smith, C. J., Kramer, R. J., Myhre, G., Forster, P. M., Soden, B. J., Andrews, T., et al. (2018).
638 Understanding Rapid Adjustments to Diverse Forcing Agents. *Geophysical Research Letters*,
639 45(21), 12,023–12,031. <https://doi.org/10.1029/2018GL079826>
640
641 Smith, C. J., Kramer, R. J., Myhre, G., Alterskjær, K., Collins, W., Sima, A., et al. (2020).
642 Effective radiative forcing and adjustments in CMIP6 models. *Atmospheric Chemistry and*
643 *Physics*, 20(16), 9591–9618. <https://doi.org/10.5194/acp-20-9591-2020>
644
645 Soden, B. J., Broccoli, A. J., & Hemler, R. S. (2004). On the Use of Cloud Forcing to Estimate
646 Cloud Feedback. *Journal of Climate*, 17(19), 3661–3665. [https://doi.org/10.1175/1520-0442\(2004\)017<3661:OTUOCF>2.0.CO;2](https://doi.org/10.1175/1520-0442(2004)017<3661:OTUOCF>2.0.CO;2)
647
648
649 Soden, B. J., Held, I. M., Colman, R., Shell, K. M., Kiehl, J. T., & Shields, C. A. (2008).
650 Quantifying Climate Feedbacks Using Radiative Kernels. *Journal of Climate*, 21(14), 3504–
651 3520. <https://doi.org/10.1175/2007JCLI2110.1>
652
653 Soden, B. J., Collins, W. D., & Feldman, D. R. (2018). Reducing uncertainties in climate models.
654 *Science*, 361(6400), 326–327. <https://doi.org/10.1126/science.aau1864>
655
656 Stier, P., Schutgens, N. A. J., Bellouin, N., Bian, H., Boucher, O., Chin, M., et al. (2013). Host
657 model uncertainties in aerosol radiative forcing estimates: results from the AeroCom Prescribed
658 intercomparison study. *Atmospheric Chemistry and Physics*, 13(6), 3245–3270.
659 <https://doi.org/10.5194/acp-13-3245-2013>

660
661 Susskind, J., Schmidt, G. A., Lee, J. N., & Iredell, L. (2019). Recent global warming as
662 confirmed by AIRS. *Environmental Research Letters*, *14*(4), 044030.
663 <https://doi.org/10.1088/1748-9326/aafd4e>
664
665 Taylor, K., Ronald, S., & Meehl, G. (2011). An overview of CMIP5 and the Experiment Design.
666 *Bulletin of the American Meteorological Society*, *93*, 485–498. [https://doi.org/10.1175/BAMS-](https://doi.org/10.1175/BAMS-D-11-00094.1)
667 [D-11-00094.1](https://doi.org/10.1175/BAMS-D-11-00094.1)
668
669 Tobin, D. C., Revercomb, H. E., Knuteson, R. O., Lesht, B. M., Strow, L. L., Hannon, S. E., et
670 al. (2006). Atmospheric Radiation Measurement site atmospheric state best estimates for
671 Atmospheric Infrared Sounder temperature and water vapor retrieval validation. *Journal of*
672 *Geophysical Research: Atmospheres*, *111*(D9). <https://doi.org/10.1029/2005JD006103>
673
674 Thorsen, T. J., Kato, S., Loeb, N. G., & Rose, F. G. (2018). Observation-Based Decomposition
675 of Radiative Perturbations and Radiative Kernels. *Journal of Climate*, *31*(24), 10039–10058.
676 <https://doi.org/10.1175/JCLI-D-18-0045.1>
677
678 Thorsen, T. J., Winker, D. M., & Ferrare, R. A. (2020). Uncertainty in observational estimates of
679 the aerosol direct radiative effect and forcing. *Journal of Climate*, 1–63.
680 <https://doi.org/10.1175/JCLI-D-19-1009.1>
681
682 Trenberth, K. E., Fasullo, J. T., & Balmaseda, M. A. (2014). Earth's Energy Imbalance. *Journal*
683 *of Climate*, *27*(9), 3129–3144. <https://doi.org/10.1175/JCLI-D-13-00294.1>
684
685 Trenberth, K. E., Zhang, Y., & Fasullo, J. T. (2015). Relationships among top-of-atmosphere
686 radiation and atmospheric state variables in observations and CESM. *Journal of Geophysical*
687 *Research: Atmospheres*, *120*(19), 10,074–10,090. <https://doi.org/10.1002/2015JD023381>
688
689 Vial, J., Dufresne, J.-L., & Bony, S. (2013). On the interpretation of inter-model spread in
690 CMIP5 climate sensitivity estimates. *Climate Dynamics*, *41*(11), 3339–3362.
691 <https://doi.org/10.1007/s00382-013-1725-9>
692
693 Watson-Parris, D., Bellouin, N., Deaconu, L. T., Schutgens, N. A. J., Yoshioka, M., Regayre, L.
694 A., et al. (2020). Constraining Uncertainty in Aerosol Direct Forcing. *Geophysical Research*
695 *Letters*, *47*(9), e2020GL087141. <https://doi.org/10.1029/2020GL087141>
696
697 Zhang, B., Kramer, R. J., & Soden, B. J. (2019). Radiative Feedbacks Associated with the
698 Madden–Julian Oscillation. *Journal of Climate*, *32*(20), 7055–7065.
699 <https://doi.org/10.1175/JCLI-D-19-0144.1>
700
701 Zhang, Q., Zheng, Y., Tong, D., Shao, M., Wang, S., Zhang, Y., et al. (2019). Drivers of
702 improved PM2.5 air quality in China from 2013 to 2017. *Proceedings of the National Academy*
703 *of Sciences*, *116*(49), 24463–24469. <https://doi.org/10.1073/pnas.1907956116>
704
705

706
707 **Figure 1.** Global-mean a) net, b) longwave (LW) and c) shortwave (SW) total radiative flux
708 anomalies from 2003 through 2018 as measured by CERES (black) and the contribution to that
709 total from the sum of radiative responses (red). Respective trendlines are displayed as dashed
710 lines. Uncertainty of $\pm 2\sigma$ is shown for each timeseries, computed as described in the Methods.
711 Linear trends and 95% confidence intervals are provided in text.

712
713 **Figure 2.** Global-mean a) total, b) longwave (LW) and c) shortwave (SW) instantaneous
714 radiative forcing (IRF) estimated from the radiative kernel technique for CERES/AIRS (red) and
715 MERRA-2 (blue). Additional calculations of greenhouse gas-only IRF are also shown using
716 empirical formulas (green) and the SOCRATES radiative transfer model (gray). For reference,
717 the trendline for total radiative flux anomalies (Fig 1a) is displayed with the total IRF as a black
718 dashed line. Uncertainty of $\pm 2\sigma$ is shown with shading for each timeseries, computed as
719 described in the Methods. Linear trends and 95% confidence intervals are provided in text and
720 in Table 1.

721
722 **Figure 3.** Local linear trends from 2003 through 2018 in all-sky shortwave instantaneous
723 radiative forcing (SW IRF) diagnosed in a) CERES/AIRS observations and b) MERRA-2
724 reanalysis using the radiative kernel differencing technique and c) from direct output of
725 MERRA-2 aerosol IRF. Also, local linear trends over the same time period are shown for aerosol
726 optical depth (AOD) from d) MODIS and e) MERRA-2.

727

728 **Table 1.** Global-mean linear trends ($\text{W/m}^2/\text{year}$) and 95% confidence bounds in instantaneous
729 radiative forcing estimated using the radiative kernel differencing technique (first two rows) and
730 MERRA-2 flux diagnostics (third row).

731